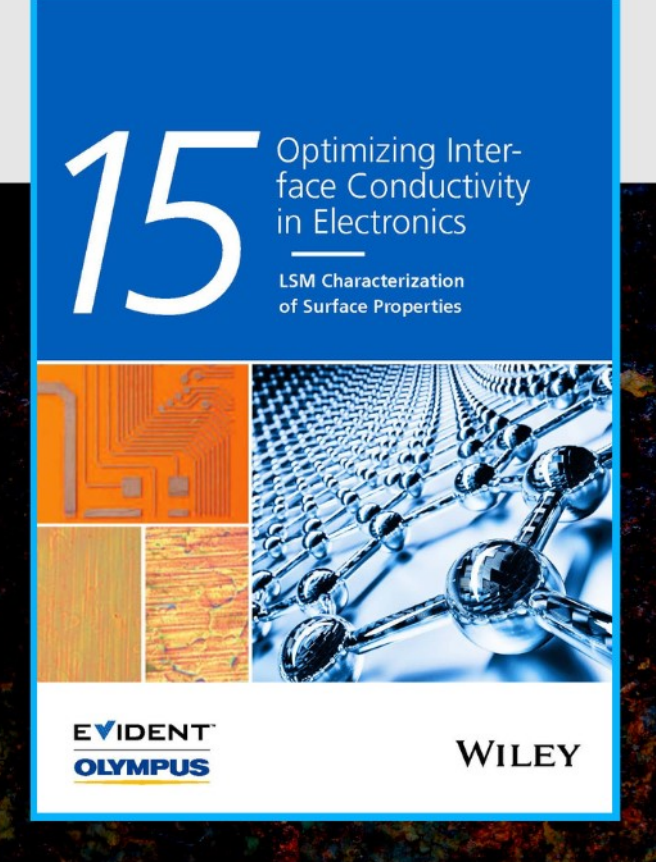


Optimizing Interface Conductivity in Electronics



The latest eBook from Advanced Optical Metrology. Download for free.

Surface roughness is a key parameter for judging the performance of a given material's surface quality for its electronic application. A powerful tool to measure surface roughness is 3D laser scanning confocal microscopy (LSM), which will allow you to assess roughness and compare production and finishing methods, and improve these methods based on mathematical models.

Focus on creating high-conductivity electronic devices with minimal power loss using laser scanning microscopy is an effective tool to discern a variety of roughness parameters.



WILEY

Check for updates

www.afm-journal.de

Origin and Energy of Intra-Gap States in Sensitive Near-Infrared Organic Photodiodes

Xiao Ma, Riccardo Ollearo, Bas T. van Gorkom, Christ H. L. Weijtens, Marco Fattori, Stefan C. J. Meskers, Albert J. J. M. van Breemen, René A. J. Janssen,* and Gerwin H. Gelinck

Trap states in organic semiconductors are notoriously detrimental to the performance of organic electronics. However, the origin and energetics of trap states remain largely elusive and under debate, especially for bulk-heterojunction (BHI) photodiodes consisting of electron donor and acceptor materials. Combining three sensitive techniques now enables locating the origin and energy of trap states in six state-of-the-art polymer non-fullerene acceptor organic photodiodes (OPDs) with noise-based specific detectivities exceeding 1013 Jones. Analyzing the temperature dependence of the reverse-bias dark current density (Jd) identifies intra-gap states in the polymers, lying 0.3-0.4 eV above the energy of the highest occupied molecular orbital, as being responsible for J_d . Sub-bandgap external quantum efficiency spectra of donor-only and acceptor-only diodes confirm that intra-gap states are much more abundant in the polymers. Likewise, responsivity measurements at ultra-low light intensities (10⁻⁷ mW cm⁻²) show trap-mediated charge recombination in BHJ and polymer-only diodes, but not in acceptor-only devices. The results imply that to further improve the specific detectivity of near-infrared OPDs, the intra-gap state energy, and density need to be reduced.

1. Introduction

Organic semiconductors (OSCs) attract considerable attention for application in displays, electronics, energy harvesting, and sensing. Their unique properties, such as mechanical flexibility and solution processing offer remarkable potential for OSCs as active materials in flexible and printable optoelectronic devices. Yet, a common challenge in these fields is the presence of trap states, a well-known factor, that significantly deteriorates device performance.[1-3] For organic photodiodes (OPDs), it is considered that trap-assisted recombination is one of the most important loss mechanisms of external quantum efficiency (EQE) at low light intensity.[4-6] Meanwhile, trapmediated thermal generation is the major contribution of reverse dark current (I_d) at low bias.[7-11] These two unfavorable traprelated phenomena strongly limit the specific detectivity (D*) of photodetectors.[4,7,8]

Unfortunately, there is only a partial understanding of the origin and the energetic distribution of trap states in OSCs. The energy of trap states remains a somewhat controversial topic for both single-carrier^[12–14] and bulk-heterojunction (BHJ) devices.^[4,7,8,15] For a range of conjugated polymers and small molecules

incorporated in single-carrier devices, universal electron, and hole trap states have been found at energies of \approx –3.6 and –6.0 eV, attributed to water-oxygen complexes and water clusters, respectively. [12,14] Traps at \approx 0.3–0.4 eV above the highest occupied molecular orbital (HOMO) and below the lowest

X. Ma, R. Ollearo, B. T. van Gorkom, C. H. L. Weijtens, S. C. J. Meskers, R. A. J. Janssen, G. H. Gelinck Molecular Materials and Nanosystems and Institute for Complex Molecular Systems

Eindhoven University of Technology P.O. Box 513, Eindhoven 5600 MB, The Netherlands

E-mail: r.a.j.janssen@tue.nl

The ORCID identification number(s) for the author(s) of this article can be found under https://doi.org/10.1002/adfm.202304863

© 2023 The Authors. Advanced Functional Materials published by Wiley-VCH GmbH. This is an open access article under the terms of the Creative Commons Attribution License, which permits use, distribution and reproduction in any medium, provided the original work is properly cited.

DOI: 10.1002/adfm.202304863

M. Fattori
Integrated Circuits
Departments of Electrical Engineering
Eindhoven University of Technology
P.O. Box 513, Eindhoven 5600 MB, The Netherlands
A. J. J. M. van Breemen, G. H. Gelinck
TNO/Holst Centre
High Tech Campus 31, Eindhoven 5656 AE, The Netherlands
R. A. J. Janssen
Dutch Institute for Fundamental Energy Research
De Zaale 20, Eindhoven 5612 AJ, The Netherlands

www.afm-journal.de

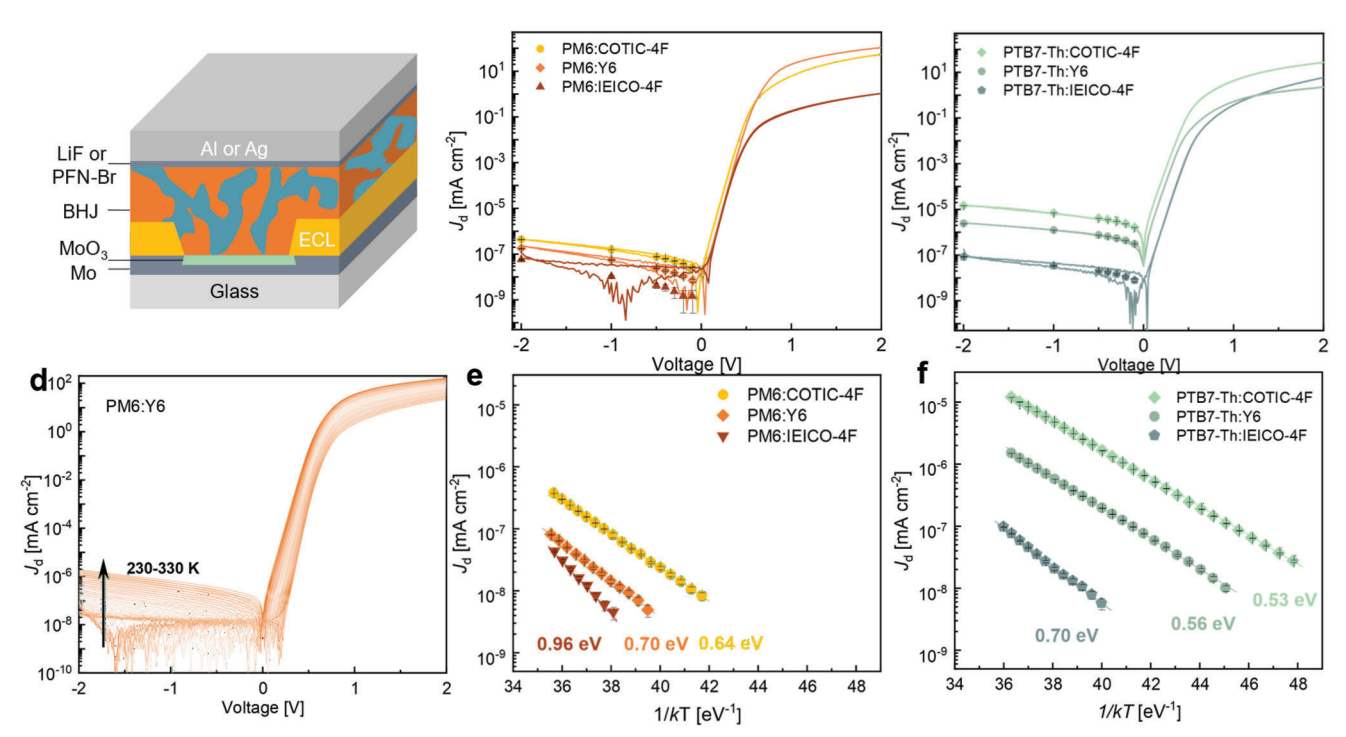


Figure 1. a) Schematic stack configuration. b,c) J-V characteristics in dark for diodes with PM6 (b) and PTB7-Th (c) blended with three NFAs (COTIC-4F, Y6, and IEICO-4F). Lines represent forward and backward voltage sweeps. Symbols represent current densities measured under constant voltage. The error bars denote the standard deviation of current during constant voltage measurement (measured over a period of 5 min). d) J-V characteristics of PM6:Y6 diode measured at different temperatures. The temperature was varied from 230 to 330 K in steps of 3 K. e,f) Arrhenius plot of the temperature dependence of the dark current density of PM6 (e) and PTB7-Th (f) diodes with the three NFAs. A voltage bias of -0.1 V was applied. Error bars on symbols are the standard deviation. Lines are best fits to the Arrhenius equation, and the corresponding activation energies are shown next to the fits.

unoccupied molecular orbital (LUMO) have been identified via trap-limited charge transport studies and ascribed to waterfilled nanovoids.[13] In organic BHJs, deep trap states located in the middle of the effective bandgap, defined as the energy difference between the acceptor LUMO ($E_{\text{LUMO,A}}$) and donor HOMO ($E_{\text{HOMO,D}}$), termed as mid-gap states, have been detected by temperature-dependent impedance spectroscopy^[7] and subbandgap EQE measurements.[8] Light intensity-dependent EQE measurements found that first-order recombination loss of photocurrent is induced by deep trap states, lying 0.35-0.6 eV below the transport level. [4] Temperature-dependent current density – voltage (I-V) characteristics show that thermal activation energy (E_a) of J_d is $\approx 0.3 - 0.5$ eV less than the effective bandgap, suggesting that I_d is not related to mid-gap states but rather originates from intra-gap states near the band edges.^[10] Considering the disordered and complex nature of BHJ blends, it has so far been very difficult to determine the origin and absolute energy of these trap states.

Herein, we investigate the origin of intra-gap states in state-of-the-art organic near-infrared (NIR) OPDs that possess low dark currents and have concomitantly high D^* up to 1.15×10^{13} Jones at 850 nm and 5.45×10^{12} Jones at 1050 nm, comparable to Si photodetectors. We investigate the temperature dependence of the dark current density, the sub-bandgap EQE, and the light-intensity dependent photocurrent for six BHJ OPDs comprising two different donor polymers and three different non-fullerene acceptors (NFAs). We find that in these OPDs E_a corresponds to the energy difference between $E_{\rm LUMO,A}$ and a (trap) energy

level at 0.3–0.4 eV above $E_{\rm HOMO,D}$ of the polymer. The results indicate that –for the materials studied– the trap states originate from the polymer. This is supported by EQE spectra of donor-only and acceptor-only diodes where sub-bandgap states are observed for the two polymers, but not for the three NFAs. Also, light intensity-dependent photocurrent ($J_{\rm ph}$) measurements at ultra-low light intensities, down to 10^{-7} mW cm⁻², reveal trapmediated recombination losses in BHJ and polymer-only devices, but not in acceptor-only devices.

2. Results and Discussion

2.1. Effect of the Acceptor on J_d and E_a in OPDs

Two series of BHJ diodes were fabricated, one using PM6 and one using PTB7-Th as donor polymer. Each polymer is combined with three NFAs: IEICO-4F, Y6, or COTIC-4F. The chemical structures and full names of the polymers and NFAs are provided in the Supporting Information (Figure S1 and Table S1, Supporting Information). These materials were chosen because their energy levels enable determining whether the activation energy of $J_{\rm d}$ is related to the bandgap of the NFA (which is the lowest in the BHJ) or to the energy difference between HOMO of donor and LUMO of acceptor. In the device stack, the photoactive BHJ layer (300 nm) was sandwiched between glass/Mo/MoO $_{\rm 3}$ and LiF/Al (or PDINO/Ag) electrodes (**Figure 1a**). To minimize leakage current between the edge of the bottom electrode and the top electrode, an edge cover layer (ECL) made of epoxy-based neg-



www.afm-journal.de

Table 1. Effective bandgap (E_g^{eff}), activation energy (E_a), acceptor LUMO energy ($E_{\text{LUMO,A}}$), and trap energy ($E_T = E_g^{\text{eff}} - E_a$) for six D–A combinations.

Donor	Acceptor	$E_{\rm g}^{ m eff}[{ m eV}]$	E _a [eV]	E _{LUMO,A} [eV]	E _{LUMO,A} — E _a [eV]	E _⊤ [eV]
PM6	COTIC-4F	0.94	0.62 ± 0.01	-4.16	-4.78	0.32
	Y6	1.00	0.66 ± 0.03	-4.10	-4.76	0.34
	IEICO-4F	1.20	0.91 ± 0.05	-3.90	-4.81	0.29
PTB7-Th	COTIC-4F	0.89	0.52 ± 0.01	-4.16	-4.68	0.37
	Y6	0.95	0.54 ± 0.01	-4.10	-4.64	0.41
	IEICO-4F	1.15	0.68 ± 0.02	-3.90	-4.58	0.47

ative photoresist (SU-8) was applied on top of the MoO₃, defining an active area of 4 mm². [16,17] Further experimental details on materials and device fabrication are provided in the Supporting Information. The *J-V* characteristics at room temperature (295 K) are shown in Figure 1b,c for the PM6- and PTB7-Th-based diodes, respectively. The solid lines represent current densities measured in forward and backward voltage scans. Symbols represent Id values measured at constant voltages. The latter is considered a more accurate way to measure low current density levels than a I-V scan because capacitive currents are minimized. [10,18,19] The I-V curves show a nearly ideal diode behavior. Under forward bias, the exponential parts of the *I*–*V* curves extend to 0 V without indication of a shunt current which may obscure intrinsic origin of I_d measured at reverse bias. In reverse bias, I_d (measured at -0.5 V) ranges from 8×10^{-8} to 4×10^{-9} mA cm⁻² and from 4×10^{-6} to 2×10^{-8} mA cm⁻², for PM6- and PTB7-Th-based diodes, respectively. In both series, I_d is reduced going from COTIC-4F, via Y6, to IEICO-4F. For each acceptor, the PM6based diode has a lower dark current than the PTB7-Th-based

Figure 1d shows the *J*–*V* characteristics of the PM6:Y6 diodes for temperatures between 230 and 330 K. The thermal activation energy E_a was determined by fitting I_d to the Arrhenius equation $(I_d \propto \exp(-E_a/kT))$ in which T is the absolute temperature and k the Boltzmann constant (Figure 1e,f). For each blend, the data can be accurately fitted with a single exponent, indicating that J_d is associated with a single thermal activation process within the temperature range studied. For PM6-based diodes, E_a (at -0.1 V) increases as the acceptor changes from COTIC-4F (0.64 eV), Y6 (0.70 eV), to IEICO-4F (0.96 eV) (Figure 1e). A similar trend is observed for PTB7-Th-based BHJs with E_a increasing from 0.53, via 0.56, to 0.70 eV (Figure 1f). To reduce the uncertainty in E_a , especially for diodes with ultra-low I_d , we determined for each D-A combination the mean E_a (Table 1) from multiple measurements of E_a for biases between -0.1 and -0.5 V, a range in which they are fairly constant (Figure S2, Supporting Information).[10]

Table 1 shows that for PM6-based OPDs, $E_{\rm a}$ is 0.32 \pm 0.03 eV less than $E_{\rm g}^{\rm eff}$ and that $E_{\rm a}$ scales linearly with $E_{\rm LUMO,A}$ for which values were taken from the literature (Figure S3 Supporting Information). [20–23] A slightly higher offset of ca. 0.42 \pm 0.05 eV with $E_{\rm g}^{\rm eff}$ is seen for PTB7-Th-based OPDs. Again $E_{\rm a}$ scales linearly with $E_{\rm LUMO,A}$. These results strongly suggest that $J_{\rm d}$ and $E_{\rm a}$ involve a transition between a localized trap state in the polymer involved and the LUMO of the acceptors.

2.2. Sub-Bandgap Transitions and Intra-Gap States in BHJ and Polymer-Only OPDs

OPDs for EQE measurements were fabricated on glass substrates, covered with patterned indium tin oxide (ITO) and a layer of PEDOT:PSS (poly(3,4-ethylenedioxythiophene) polystyrene sulfonate). After depositing the photoactive layer, a LiF/Al (or PDINO/Ag) electrode was applied. EQE spectra measured for donor-only (Figure 2a) and acceptor-only diodes (Figure 2b) show that photoexcitation of the pure materials above the optical bandgaps results in photocurrent, albeit with a relatively low EQE of 10^{-3} to 10^{-2} . In addition, the sensitive EQE spectra of PM6-only and PTB7-Th-only diodes also show a distinct photoresponse below the optical bandgap, indicating the presence of intra-gap states contributing to the photocurrent in the polymers (Figure 2a), down to photon energies of 0.80 and 0.65 eV for PM6 and PTB7-Th, respectively. In contrast, for the three NFA-only diodes there is no clear evidence of charge generation when they are photoexcited below the optical bandgap (Figure 2b). For the NFAs, the EQE decays exponentially below the band edge until it approaches the noise level ($\approx 1 \times 10^{-8}$) at photon energies of ≈0.85 eV (COTIC-4F), 0.93 eV (Y6), and 0.95 eV (IEICO-4F).

Therefore, we conclude that the intra-gap states that are responsible for I_d as well as low-energy optical charge generation in the BHJ OPDs primarily originate from the polymer and, thus consider that the activation energy Ea corresponds to the energy difference between the intra-gap states in the donor and the LUMO of the acceptor. This process is schematically shown in Figure 2c, where the grey curves and lines within the bandgap of donor and acceptor schematically illustrate the hypothetical density distribution of intra-gap states as a function of energy. In this embodiment, the absolute energy of the intra-trap states responsible for $J_{\rm d}$ corresponds to $E_{\rm LUMO,A}-E_{\rm a}.$ The colored markers in Figure 2d show the location of $E_{\text{LUMO,A}} - E_{\text{a}}$ for each D-A combination. For the three PM6-based diodes, these are in a narrow range of -4.78 ± 0.03 eV (Table 1). This indicates that the same intra-gap state in PM6 determines the I_d for each blend. Similarly, for PTB7-Th-based BHJs, the intra-gap states are located at an energy of -4.63 ± 0.05 eV (Table 1).

Using the $E_{\rm HOMO,D}$ of PM6 and PTB7-Th, determined by ultraviolet photoelectron spectroscopy (UPS) (Figures S3 and S4, Supporting Information), the energies of the intra-gap states relative to the HOMO levels are given by $E_{\rm T}=E_{\rm g}^{\rm eff}-E_{\rm a}$, and found to be $E_{\rm T}=0.32\pm0.03$ eV for PM6 and $E_{\rm T}=0.42\pm0.05$ eV for PTB7-Th (Table 1).

www.afm-journal.de

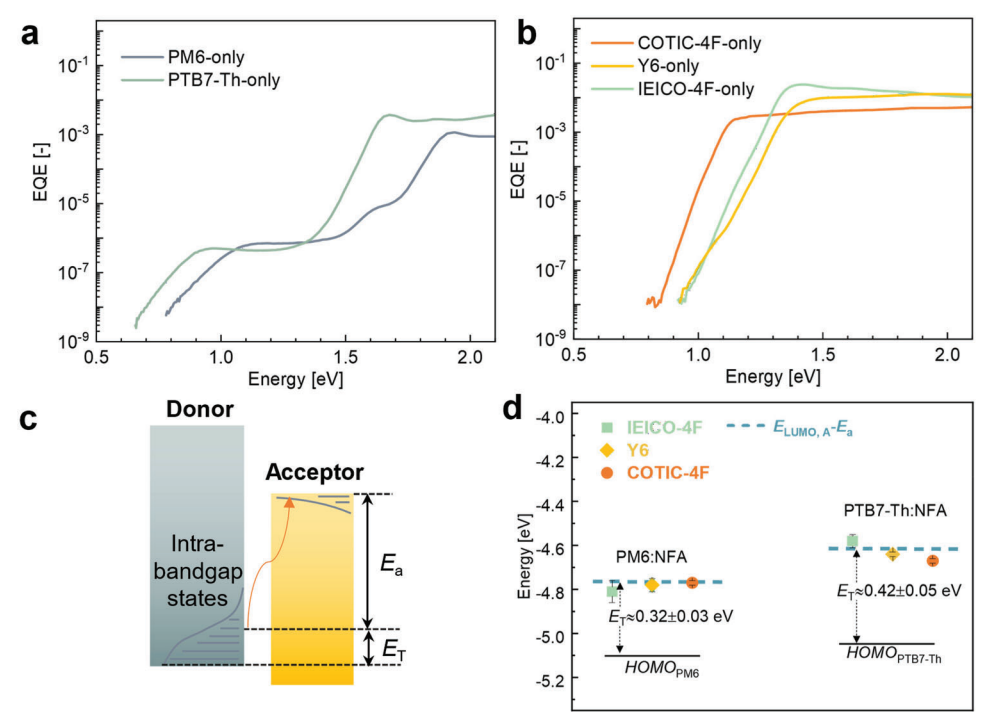


Figure 2. a–b) Comparison of EQE spectra of single-component diodes with a bottom transparent device stack of ITO/MoO₃/photoactive layer/LiF/Al polymer donor-only diodes (a) and NFA-only diodes (b). c) Schematic plot shows the mechanism of thermal generation current mediated by the intragap states in donor above its HOMO. Grey curves and horizontal lines within the bandgap illustrate the hypothetical density distribution of trap states related to J_d . d) Energy diagrams comparing the energies of trap states determined by $E_{LUMO,A}$ minus E_a for two groups of BHJs. Squares, diamonds, and circles stand for IEICO-4F, Y6, and COTIC-4F based BHJs, respectively. For PM6-based and PTB7-Th-based diodes, BHJs with three different NFAs reveal a consistent trap depth level at 0.32 ± 0.03 eV and 0.42 ± 0.05 eV above the polymer HOMO level, respectively.

2.3. Trap-Mediated Recombination at Ultra-Low Light Intensity

Figure 3a shows the light intensity (I_I) dependent photocurrent density (J_{ph}) recorded at 540 nm for PM6:Y6 and PTB7-Th:IEICO-4F photodiodes consisting of a glass/Mo/MoO₃/activate layer/AZO/ITO device stack to enable top illumination. At each light intensity, $J_{\rm ph}$ was determined in direct current mode by averaging the photocurrent for 5 min at 0 V bias. [4,24] The correlation between $J_{\rm ph}$ and $I_{\rm L}$ in a doublelogarithmic plot suggests a linear dynamic range extending over almost nine orders of magnitude in light intensity, from 10⁻⁷ to 10² mW cm⁻². Closer inspection, however, in the form of a responsivity ($R = J_{\rm ph}/I_{\rm L}$) plot as a function of light intensity (Figure 3b), reveals nonlinear behavior at high and ultralow light conditions. R first gradually increases with light intensity, then reaches a plateau at moderate light intensities (10^{-3} to 1 mW cm⁻²), and subsequently decreases steeply for light intensities above ≈ 1 mW cm⁻². The decrease of the responsivity at high light intensities is well known and can be attributed to bimolecular (Langevin-type) recombination.[4,15,25,26] The initial increase of R with increasing light intensities at intensities below 10⁻⁴ mW cm⁻² is rarely reported or discussed in previous work, mostly because of the lack of photocurrent measurement at intensities below 10⁻⁴ mW cm⁻².[4,15,24,25,27-29] Only a few studies reported this phenomenon,[5,6,24,30,31] and attributed it to trap-related recombination. Liraz et al.[24] explained it by the role of excess of charges that have diffused from the contact into the semiconductor and fill defect states. At low light intensities,

these recombine with photogenerated carriers, while at higher intensities the density of photocarriers exceed that of trapped carriers, thereby increasing *R*. Hartnagel and Kirchartz^[32] used drift-diffusion modeling and found that under low illumination, the trapped charge density decreases with light intensity while the photogenerated carrier density increases linearly, causing a sublinear recombination rate and resulting in an increasing responsivity at higher light intensities.

Figure 3c,d shows the normalized responsivity of BHJ and single-component, i.e., donor-only or acceptor-only, diodes between 10^{-7} and $\approx 10^{-2}$ mW cm⁻². Because free charge generation is strongly reduced in the single component diodes (Figure S5, Supporting Information), $J_{\rm ph}$ was too small to be measured at light intensities below 10⁻⁷ mW cm⁻². For PM6-only and PTB7-Th-only diodes, an increase of the responsivity is observed at low light intensities (10^{-5} to $\approx 10^{-3}$ mW cm⁻²), similar to what is seen in BHJs at lower light intensities (10^{-7} to 10^{-3} mW cm⁻²). We attribute this effect to trap-related recombination losses, signaling the presence of intra-gap states in the polymers. Above 10⁻³ mW cm⁻², the responsivity reaches a plateau. In contrast, for Y6-only devices, the responsivity remains constant for light intensities between 10⁻⁵ and 10⁻² mW cm⁻² (Figure 3c). This suggests that trap-related recombination is negligible in Y6-only diodes. Due to a poor morphology of IEICO-4F-only films, relatively high dark currents were recorded that precluded measuring a photocurrent in direct current mode at low light intensities. Hence, its light intensity-dependent photocurrent could not be studied.

www.afm-journal.de

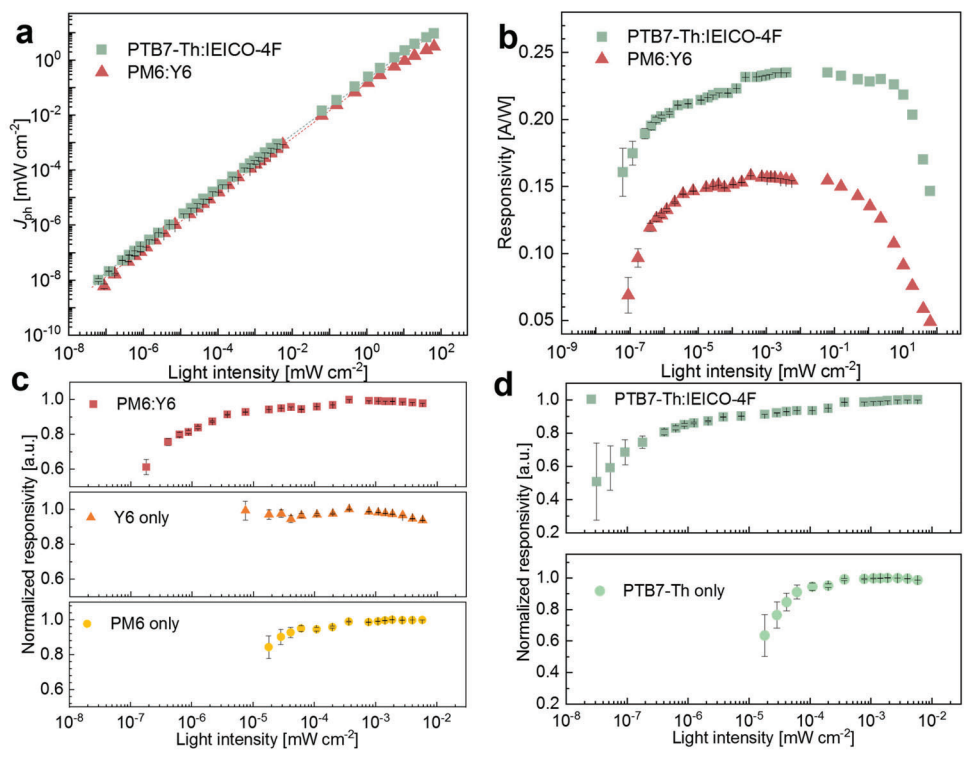


Figure 3. a) Short-circuit photocurrent of PM6:Y6 and PTB7-Th:IEICO-4F BHJ diodes as function of light intensity. The following device stack was used: Mo/MoO₃/photoactive layer/AZO/ITO with ECL. Illumination was from the top (ITO side) using a calibrated 540 nm LED as light source. b) Responsivity as a function of light intensity of the photodiodes in (a). c) Normalized responsivity plotted as a function of light intensity for PM6:Y6 BHJ and single-component (Y6-only and PM6-only) diodes. d) Normalized responsivity plotted as a function of light intensity for PTB7-Th:IEICO-4F BHJ and PTB7-Th single-component diodes.

The increasing responsivity of PTB7-Th:IEICO-4F OPD with light intensity at low light, intensities occurs at different temperatures (205, 250, and 295 K) (Figure S6, Supporting Information). The responsivity increases slightly with temperature, which is a sign of more efficient charge extraction, probably associated with the higher mobilities at higher temperatures.^[33]

The light intensity-dependent photocurrent and ultra-sensitive EQE measurement corroborate, independently, that intra-gap states in the polymer are the main contribution to the intra-gap states in BHJs.

2.4. Characterization of the Overall Performance of the Near-Infrared OPDs

Figure 4a,b shows the spectral responsivity at −1 V of the six BHJ OPDs. The corresponding EQE spectra are shown in Figure S7 (Supporting Information). Each of PTB7-Th-based OPDs gives rise to a significant responsivity, R > 0.3 A W $^{-1}$ for COTIC-4F and Y6, and R > 0.4 A W $^{-1}$ for IEICO-4F, extending to 1110, 920, and 970 nm, respectively, depending on the optical bandgap of the NFA. For the PM6-based OPDs the responsivity is lower in combination with COTIC-4F and IEICO-4F (R < 0.1 A W $^{-1}$), but not for Y6 where R > 0.3 A W $^{-1}$. The low responsivity for PM6 in combination with COTIC-4F and IEICO-4F is due to the relatively low ionization energy (IE) offset^[23] in these diodes, which limits charge generation (Figure S3, Supporting Information).

Interestingly, the responsivity spectra of PM6:Y6 and PTB7-Th:Y6 OPDs are similar in shape and value (Figure 4a,b). The dark current of the former, however, is more than one order of magnitude lower (Figure 1e,f). We attribute this to the fact that the trap states in PM6 (at -4.76 eV) lie deeper than those in PTB7-Th (at \approx 4.64 eV). This demonstrates that it is possible to achieve a lower dark current but retain the responsivity in the NIR by selecting a donor with deep-lying intra-gap states. To better demonstrate this, we consider the specific detectivity (D^*) which is an important figure of merit for photodetectors and is defined by D^* = $R(AB)^{1/2}/i_n$, where A is the device area, B is bandwidth, and $i_{\rm n}$ is the noise current of the devices. The current noise spectral densities (1-100 Hz) of four OPDs measured at -1 V are compared in Figure 4c with a bandwidth of 1 Hz. The noise current densities at -0.5 and -1 V are shown in Figure S8 (Supporting Information) for all D–A combinations. Figure 4c shows a clear decrease in noise current for the PTB7-Th-based OPDs, going from COTIC-4F, via Y6, to IEICO-4F following the trend in the dark currents (Figure 1f). A frequency-dependent (1/f) behavior of i_n between 1 and 10 Hz is observed. Above 10 Hz, the noise currents converge to a plateau with average values of 8.80×10^{-15} , 8.28×10^{-15} , and 7.45×10^{-15} A Hz^{-1/2}, respectively, very close to the noise floor (6.0 \times 10⁻¹⁵ A Hz^{-1/2}) of the setup. Considering that the reverse dark current for PTB7-Th:COTIC-4F is about two orders of magnitude higher than for PTB7-Th:IEICO-4F, the difference between their measured noise currents at 1 Hz is rather small, only less than a factor of 2. The shot noise $(i_{n,s})$ is given

www.afm-journal.de

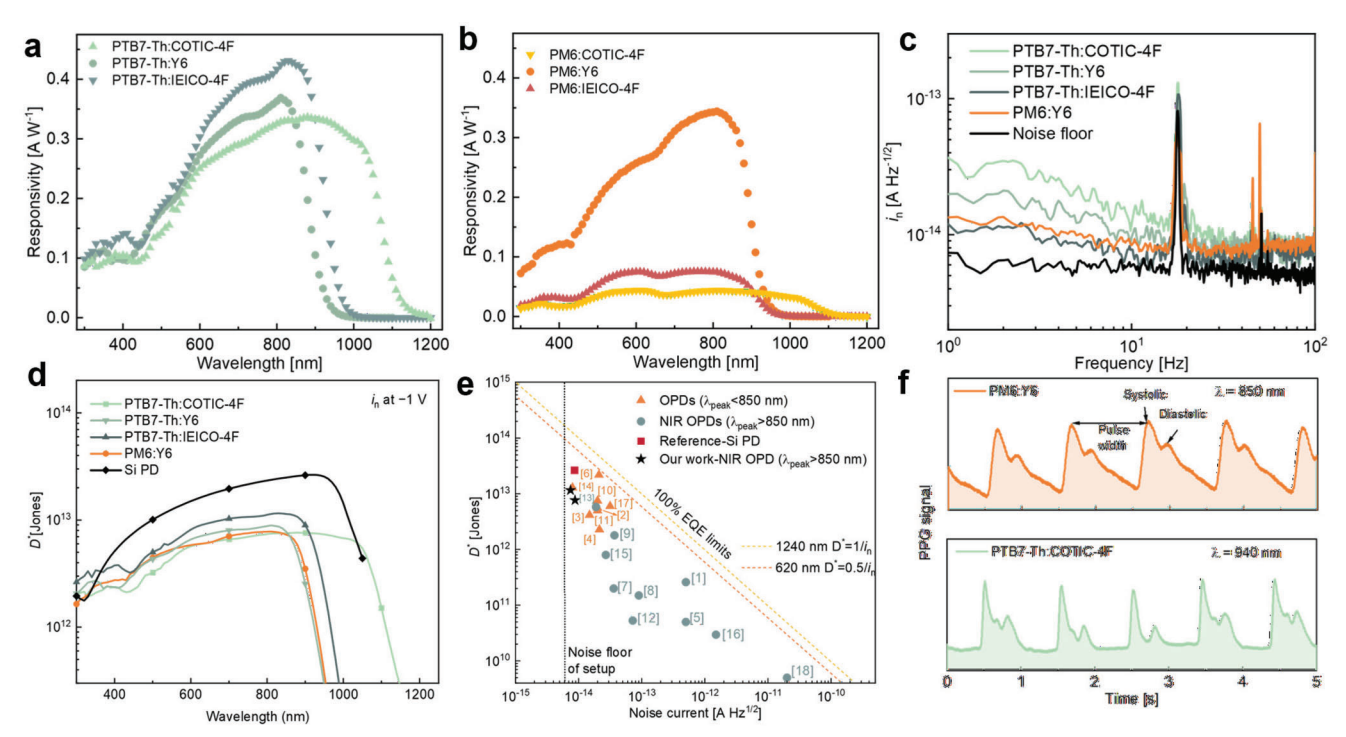


Figure 4. a-b) Responsivity at $-1\,\text{V}$ versus wavelength for OPDs with a Mo/MoO₃/photoactive layer/AZO/ITO device stack (with ECL) for PTB7-Th:NFA (a) and PM6:NFA (b) BHJ blends. c) Noise current spectral density as a function of frequency measured at $-1\,\text{V}$. d) Specific detectivity of the NIR OPDs at different wavelength under reverse bias of $-1\,\text{V}$. e) Comparison of specific detectivity between reported values and measured values in this work (PTB7-Th:IEICO-4F at 850 nm, PTB7-Th:COTIC-4F at 1050 nm) as a function of measured noise current (see Table S2, Supporting Information for details). Grey triangles represent D^* values taken from reports that use measured noise currents. The 100% EQE limits lines provide the highest possible as function of the noise current. Different colors denote a certain optical bandgap, indicated in the legend. The vertical dotted line represents the noise floor of the noise measurement setup. f) PPG signal measured in transmission mode through a human finger. The typical PPG waveform measured by PM6:Y6 and PTB7-Th:COTIC-4F OPDs under near-infrared light with wavelength of 850 and 940 nm, respectively. The systolic and diastolic peaks and pulse width are noted with dark arrows.

by $i_{\rm n,s}=(2qBJ_{\rm d})^{1/2}$ and calculated to be 4.7×10^{-15} , 2.0×10^{-15} , and 3.3×10^{-16} A Hz^{-1/2} for three PTB7-Th-based OPDs. The calculated shot noise $i_{\rm n,s}$ is therefore much smaller than both the actual $i_{\rm n}$ and the noise floor, illustrating that other noise sources, such as for instance the observed 1/f noise, are dominant in our OPDs.

The specific detectivity (D^*) spectra at -1 V determined from R and i_n (the average value between 10 to 100 Hz is taken) are shown in Figure 4d. The three OPDs based on PTB7-Th demonstrate a peak detectivities of 1.15×10^{13} (850 nm) (IECO-4F), 8.77 $\times 10^{12}$ (800 nm) (Y6), and 5.45 $\times 10^{12}$ Jones (1050 nm) (COTIC-4F). While for PM6:Y6 the D^* equals 7.78×10^{12} (800 nm). These values are among the highest reported noise current-based detectivities for OPDs and close to that of a commercial Si PD (Thorlabs FDS100) with $D^* > 1.0 \times 10^{13}$ Jones between 600 and 1050 nm. Figure 4e shows D^* values of broadband OPDs as a function of noise current extracted from the literature, and the overview of figure-of-merits can be found in Table S2 (Supporting Information).^[5-7,20,34-50] Here, we only selected reports that use measured noise current to calculate the specific detectivity, because the calculation based on thermal and shot noise (derived from I_d) leads to an overestimation of D^* .[31,48] The dotted lines denote the expected D^* as a function of i_n for hypothetical devices with 100% EQE at wavelength of 620 and 1240 nm. All the OPDs cited here show a *D** below these dotted lines, including the lownoise Si photodiode ($R = 0.65 \text{ A W}^{-1}$, $A = 0.13 \text{ cm}^2$). The dark dotted line represents the noise floor of our noise measurement setup ($6.0 \times 10^{-15} \text{ A Hz}^{-1/2}$) (Table S2, Supporting Information).

To demonstrate the potential application of the NIR OPDs developed in this work, we selected photoplethysmography (PPG). PPG optically detects in volume changes in subcutaneous tissue caused by blood pulses and requires sensitivity in the NIR region Figure 4f shows the PPG signal measured on a finger of one of the authors by OPDs in transmission mode under NIR light with wavelength of 850 and 940 nm. A heart rate of 57–62 bpm can be easily determined, and also the higher-order features such as the systolic and diastolic peaks are readily discerned in the PPG waveform, demonstrating a high-quality OPD.

3. Conclusions

The reverse dark current in the six studied polymer:NFA OPDs originates from thermal charge generation from an intra-gap state in the donor polymer to the LUMO of the NFA. The energy of the intra-gap state is $\approx\!0.3$ eV above the HOMO in PM6 and $\approx\!0.4$ eV in PTB7-Th. Sub-bandgap features in the ultra-sensitive EQE spectra of the polymers and responsivity measurements at ultra-low light intensities confirm that sub-bandgap states and trap-related recombination are evident in BHJ and polymer-only diodes, while not observed for the NFA-only diodes.



www.afm-journal.de

The intrinsic nature and density of trap states in polymers is still unknown and further research is needed to clarify this aspect. The trap states might be due to impurities (e.g., water, oxygen, metals, remnant materials from synthesis) but can also involve structural changes of the semiconductors that formed during synthesis or work-up. The fact that intra-gap states in the polymers limit the specific detectivity of OPDs, suggests that further improvements should focus on lowering the energy depth of these states or reducing their density, for instance, via improving material purity. Nevertheless, it is encouraging that OPDs even with evident intra-gap states, noise-current-based specific detectivities close to 10^{13} Jones can be achieved in the spectral range between 600 and 1050 nm, comparable to that of a state-of-the-art Si photodiode, while PPG signal measurements illustrate their potential healthcare applications.

4. Experimental Section

OPD Fabrication: Details of materials and device fabrication are provided in the Supporting Information.

Ultraviolet Photoelectron Spectroscopy: The UPS measurements were performed with a VG EscaLab II system under a base pressure of 10^{-8} Pa. He–I radiation of 21.22 eV and a bias of -6 V were used during measurement.

Temperature Dependent Current: J-V characteristics were measured in a high vacuum (10^{-4} mbar) probe station equipped with triaxial probe arms (Janis Research, Model ST-500-2-(6TX)) in which the temperature was controlled by a Lake Shore 336 temperature controller. A LabView code was used to program the temperature and source meter (Keithley 2636A). J-V characteristics were measured with voltage steps of 1 mV. Current density at different temperatures was recorded for a given voltage, by recording the current for 5 min. The average value of the last minute was defined as the current density. Opaque electrodes were chosen to eliminate any effect of stray light on the reverse current.

Ultrasensitive EQE: The setup for sub-bandgap EQE spectroscopy consisted of a tungsten-halogen lamp (250 W), a chopper (Oriel 3502), a monochromator (Oriel, Cornerstone 260), a preamplifier (Stanford Research Systems SR570), and a lock-in amplifier (Stanford Research SR830). A series of long pass filters with increasing cut-on wavelengths was placed between the lamp and monochromator to remove stray light during the measurement. The monochromatic light is then passed through a concave cylindrical lens, to focus the light and increase the intensity on the active area of the solar cell. Reference Si and InGaAs photodiodes were used to calibrate the incident light intensity. The OPDs were held in a home-built cell holder filled with $\rm N_2$. The OPDs had a transparent ITO front electrode, a metal (Al or Ag) back electrode, and were contacted the backside of glass substrate.

Noise Measurements: A battery-powered current-to-voltage conversion readout circuit is developed with off-the-shelf components. The setup is integrated in a metal enclosure to shield from electromagnetic

interference. The diodes were connected to a trans-impedance amplifier (TIA) implemented with an operational amplifier (Analog Devices ADA4530). An adjustable DC voltage source was applied to the non-inverting terminal of the TIA to modify the bias of device. The output of the TIA was fed to an active bandpass amplifier (implemented with the Analog Devices AD8065) and read out by a dynamic signal analyzer (HP35670A).

Photoplethysmography Signal Measurements: The OPD was connected to probes integrated into a custom-made sample holder. The probes were then connected to a signal amplifier (Stanford Research Systems, SR570), a lock-in amplifier (Stanford Research Systems, SR830 DSP), and an oscilloscope (Tektronix, TDS3032B). The light sources (NIR LEDs at 940 or 850 nm) were powered by a wave function generator (PeakTech, 4040), and positioned at 1 or 2 cm above the finger. The NIR OPD with protective lamination was placed ≈1.5 cm below the finger. During the acquisition of PPG signal, raw signals were electronically filtered using a band-pass digital filter from 0.5 to 10 Hz to remove the out-of-band and nonpulsatile (DC) components.

Supporting Information

Supporting Information is available from the Wiley Online Library or from the author.

Acknowledgements

The authors thank the process engineers of Holst Centre's R&D Pilot Line for the fabrication of the OPD substrates. The authors acknowledge funding from the Ministry of Education, Culture, and Science (Gravity program 024.001.035) and from Netherlands Organisation for Scientific Research (NWO Spinoza grant). The work is further part of the Advanced Research Center for Chemical Building Blocks, ARC CBBC, which is co-founded and co-financed by Netherlands Organisation for Scientific Research (NWO) and the Netherlands Ministry of Economic Affairs (project 2016.03.Tue).

Conflict of Interest

The authors declare no conflict of interest.

Author Contributions

X.M. fabricated and characterized the devices. R.O. performed with PPG measurement. B.T.v.G. performed sensitive EQE measurements. C.H.L.W performed UPS experiments. M.F. developed the noise setup. A.J.J.M.v.B. optimized the processes of OPD substrates. X.M., R.O., S.C.J M., R.A.J.J., and G.H.G. planned the research and interpreted the data. X.M. wrote the manuscript with help of R.A. J.J. and G.H.G. All authors commented on it

Data Availability Statement

The data that support the findings of this study are available from the corresponding author upon reasonable request.

Keywords

bulk-heterojunctions, near-infrared photodiodes, noise current, organic semiconductors, trap states

Received: May 3, 2023 Revised: July 2, 2023 Published online:



www.afm-journal.de

- [1] P. W. M. Blom, Adv. Mater. Technol. 2020, 5, 2000144.
- [2] J. Yuan, C. Zhang, B. Qiu, W. Liu, S. K. So, M. Mainville, M. Leclerc, S. Shoaee, D. Neher, Y. Zou, *Energy Environ. Sci.* **2022**, *15*, 2806.
- [3] H. F. Haneef, A. M. Zeidell, O. D. Jurchescu, J. Mater. Chem. C 2020, 8, 759.
- [4] S. Zeiske, O. J. Sandberg, N. Zarrabi, W. Li, P. Meredith, A. Armin, Nat. Commun. 2021, 12, 3603.
- [5] C. Fuentes-Hernandez, W.-F. Chou, T. M. Khan, L. Diniz, J. Lukens, F. A. Larrain, V. A. Rodriguez-Toro, B. Kippelen, *Science* 2020, 370, 698.
- [6] Y. Park, C. Fuentes-Hernandez, K. Kim, W.-F. Chou, F. A. Larrain, S. Graham, O. N. Pierron, B. Kippelen, Sci. Adv. 2021, 7, eabi6565.
- [7] J. Kublitski, A. Hofacker, B. K. Boroujeni, J. Benduhn, V. C. Nikolis, C. Kaiser, D. Spoltore, H. Kleemann, A. Fischer, F. Ellinger, K. Vandewal, K. Leo. Nat. Commun. 2021, 12, 551.
- [8] N. Zarrabi, O. J. Sandberg, S. Zeiske, W. Li, D. B. Riley, P. Meredith, A. Armin, Nat. Commun. 2020, 11, 5567.
- [9] A. H. Fallahpour, S. Kienitz, P. Lugli, IEEE Trans. Electron Devices 2017, 64, 2649.
- [10] X. Ma, H. Bin, B. T. van Gorkom, T. P. A. van der Pol, M. J. Dyson, C. H. L. Weijtens, M. Fattori, S. C. J. Meskers, A. J. J. M. van Breemen, D. Tordera, R. A. J. Janssen, G. H. Gelinck, Adv. Mater. 2022, 2209598.
- [11] O. J. Sandberg, C. Kaiser, S. Zeiske, N. Zarrabi, S. Gielen, W. Maes, K. Vandewal, P. Meredith, A. Armin, Nat. Photonics 2023, 17, 368.
- [12] H. T. Nicolai, M. Kuik, G. Wetzelaer, B. de Boer, C. Campbell, C. Risko, J. L. Brédas, P. W. M. Blom, Nat. Mater. 2012, 11, 882.
- [13] G. Zuo, M. Linares, T. Upreti, M. Kemerink, Nat. Mater. 2019, 18, 588.
- [14] N. B. Kotadiya, A. Mondal, P. W. M. Blom, D. Andrienko, G.-J. A. H. Wetzelaer, *Nat. Mater.* **2019**, *18*, 1182.
- [15] C. Labanti, J. Wu, J. Shin, S. Limbu, S. Yun, F. Fang, S. Y. Park, C.-J. Heo, Y. Lim, T. Choi, H.-J. Kim, H. Hong, B. Choi, K.-B. Park, J. R. Durrant, J.-S. Kim, *Nat. Commun.* 2022, 13, 3745.
- [16] G. Simone, M. J. Dyson, C. H. L. Weijtens, S. C. J. Meskers, R. Coehoorn, R. A. J. Janssen, G. H. Gelinck, Adv. Opt. Mater. 2020, 8, 1901568.
- [17] D. Tordera, B. Peeters, H. B. Akkerman, A. J. J. M. van Breemen, J. Maas, S. Shanmugam, A. J. Kronemeijer, G. H. Gelinck, Adv. Mater. Technol. 2019, 4, 1900651.
- [18] A. J. J. M. van Breemen, R. Ollearo, S. Shanmugam, B. Peeters, L. C. J. M. Peters, R. L. van de Ketterij, I. Katsouras, H. B. Akkerman, C. H. Frijters, F. Di Giacomo, S. Veenstra, R. Andriessen, R. A. J. Janssen, E. A. Meulenkamp, G. H. Gelinck, *Nat. Electron.* 2021, 4, 818.
- [19] R. Ollearo, J. Wang, M. J. Dyson, C. H. L. Weijtens, M. Fattori, B. T. van Gorkom, A. J. J. M. van Breemen, S. C. J. Meskers, R. A. J. Janssen, G. H. Gelinck, *Nat. Commun.* 2021, 12, 7277.
- [20] Y. Song, Z. Zhong, P. He, G. Yu, Q. Xue, L. Lan, F. Huang, Adv. Mater. 2022, 34, 2201827.
- [21] J. Lee, S.-J. Ko, M. Seifrid, H. Lee, B. R. Luginbuhl, A. Karki, M. Ford, K. Rosenthal, K. Cho, T.-Q. Nguyen, G. C. Bazan, Adv. Energy Mater. 2018, 8, 1801212.
- [22] V. V. Brus, N. Schopp, S.-J. Ko, J. Vollbrecht, J. Lee, A. Karki, G. C. Bazan, T.-Q. Nguyen, Adv. Energy Mater. 2021, 11, 2003091.
- [23] S. Karuthedath, J. Gorenflot, Y. Firdaus, N. Chaturvedi, C. S. P. De Castro, G. T. Harrison, J. I. Khan, A. Markina, A. H. Balawi, T. A. D. Peña, W. Liu, R.-Z. Liang, A. Sharma, S. H. K. Paleti, W. Zhang, Y. Lin, E. Alarousu, S. Lopatin, D. H. Anjum, P. M. Beaujuge, S. De Wolf, I. McCulloch, T. D. Anthopoulos, D. Baran, D. Andrienko, F. Laquai, Nat. Mater. 2021, 20, 378.
- [24] D. Liraz, P. Cheng, Y. Yang, N. Tessler, J. Appl. Phys. 2022, 131, 135501.

- [25] M. Stolterfoht, B. Philippa, S. Shoaee, H. Jin, W. Jiang, R. D. White, P. L. Burn, P. Meredith, A. Pivrikas, J. Phys. Chem. C 2015, 119, 26866.
- [26] J. Wu, J. Luke, H. K. H. Lee, P. Shakya Tuladhar, H. Cha, S.-Y. Jang, W. C. Tsoi, M. Heeney, H. Kang, K. Lee, T. Kirchartz, J.-S. Kim, J. R. Durrant, Nat. Commun. 2019, 10, 5159.
- [27] M. Stolterfoht, S. Shoaee, A. Armin, H. Jin, I. Kassal, W. Jiang, P. Burn, P. Meredith, Adv. Energy Mater. 2017, 7, 1601379.
- [28] Q. Liu, S. Zeiske, X. Jiang, D. Desta, S. Mertens, S. Gielen, R. Shanivarasanthe, H.-G. Boyen, A. Armin, K. Vandewal, *Nat. Commun.* 2022, 13, 5194.
- [29] L. Tzabari, N. Tessler, J. Appl. Phys. 2011, 109, 064501.
- [30] F. Guo, B. Yang, Y. Yuan, Z. Xiao, Q. Dong, Y. Bi, J. Huang, Nat. Nanotechnol. 2012, 7, 798.
- [31] Y. Fang, A. Armin, P. Meredith, J. Huang, Nat. Photonics 2019, 13, 1.
- [32] P. Hartnagel, T. Kirchartz, Adv Theory Simul 2020, 3, 2000116.
- [33] W. F. Pasveer, J. Cottaar, C. Tanase, R. Coehoorn, P. A. Bobbert, P. W. M. Blom, D. M. de Leeuw, M. A. J. Michels, *Phys. Rev. Lett.* 2005, 94, 206601.
- [34] Y. Yao, Y. Liang, V. Shrotriya, S. Xiao, L. Yu, Y. Yang, Adv. Mater. 2007, 19, 3979.
- [35] L. Zhang, T. Yang, L. Shen, Y. Fang, L. Dang, N. Zhou, X. Guo, Z. Hong, Y. Yang, H. Wu, J. Huang, Y. Liang, Adv. Mater. 2015, 27, 6496.
- [36] S. Xiong, L. Li, F. Qin, L. Mao, B. Luo, Y. Jiang, Z. Li, J. Huang, Y. Zhou, ACS Appl. Mater. Interfaces 2017, 9, 9176.
- [37] Z. Wu, W. Yao, A. E. London, J. D. Azoulay, T. N. Ng, Adv. Funct. Mater. 2018, 28, 1800391
- [38] S. Gielen, C. Kaiser, F. Verstraeten, J. Kublitski, J. Benduhn, D. Spoltore, P. Verstappen, W. Maes, P. Meredith, A. Armin, K. Vandewal, Adv. Mater. 2020, 32, 2003818.
- [39] Z. Huang, Z. Zhong, F. Peng, L. Ying, G. Yu, F. Huang, Y. Cao, ACS Appl. Mater. Interfaces 2021, 13, 1027.
- [40] Z. Wu, N. Li, N. Eedugurala, J. D. Azoulay, D.-S. Leem, T. N. Ng, Npj Flex Electron 2020, 4, 6.
- [41] J. Huang, J. Lee, H. Nakayama, M. Schrock, D. X. Cao, K. Cho, G. C. Bazan, T.-Q. Nguyen, ACS Nano 2021, 15, 1753.
- [42] W. Yang, W. Qiu, E. Georgitzikis, E. Simoen, J. Serron, J. Lee, I. Lieberman, D. Cheyns, P. Malinowski, J. Genoe, H. Chen, P. Heremans, ACS Appl. Mater. Interfaces 2021, 13, 16766.
- [43] P. Jacoutot, A. D. Scaccabarozzi, T. Zhang, Z. Qiao, F. Aniés, M. Neophytou, H. Bristow, R. Kumar, M. Moser, A. D. Nega, A. Schiza, A. Dimitrakopoulou-Strauss, V. G. Gregoriou, T. D. Anthopoulos, M. Heeney, I. McCulloch, A. A. Bakulin, C. L. Chochos, N. Gasparini, Small 2022. 18. 2200580.
- [44] I. Park, C. Kim, R. Kim, N. Li, J. Lee, O. K. Kwon, B. Choi, T. N. Ng, D.-S. Leem, Adv. Opt. Mater. 2022, 10, 2200747.
- [45] Y. Zheng, Y. Chen, Y. Cao, F. Huang, Y. Guo, X. Zhu, ACS Mater. Lett. 2022. 4, 882.
- [46] M. Biele, C. M. Benavides, J. Hürdler, S. F. Tedde, C. J. Brabec, O. Schmidt, Adv. Mater. Technol. 2019, 4, 1800158.
- [47] A. J. J. M. van Breemen, M. Simon, O. Tousignant, S. Shanmugam, J.-L. van der Steen, H. B. Akkerman, A. Kronemeijer, W. Ruetten, R. Raaijmakers, L. Alving, J. Jacobs, P. E. Malinowski, F. De Roose, G. H. Gelinck, Npj Flex Electron 2020, 4, 22.
- [48] J. Vanderspikken, W. Maes, K. Vandewal, Adv. Funct. Mater. 2021, 31, 2104060.
- [49] H. Lin, B. Xu, J. Wang, X. Yu, X. Du, C.-J. Zheng, S. Tao, ACS Appl. Mater. Interfaces 2022, 14, 34891.
- [50] S. Xiong, J. Li, J. Peng, X. Dong, F. Qin, W. Wang, L. Sun, Y. Xu, Q. Lin, Y. Zhou, Adv. Opt. Mater. 2022, 10, 2101837.